MASTERS BY RESEARCH

Wind driven energy flows as a micro-renewable resource

Kennington, Michael

Award date:
2023

Awarding institution:
Bangor University

Wind driven energy flows as a micro-renewable resource

Name: M. Kennington

Student ID number: 500418918

I hereby declare that this thesis is the results of my own investigations, except where otherwise stated. All other sources are acknowledged by bibliographic references. This work has not previously been accepted in substance for any degree and is not being concurrently submitted in candidature for any degree unless, as agreed by the University, for approved dual awards.

Wind driven energy flows as a micro-renewable resource

Author M. Kennington

Author affiliations: Bangor University, KESS2 research program

Abstract

Buoy observation platforms require energy. Modern advances in equipment power efficiency and advances such as the Self-Contained Ocean Observation Payload systems collecting real time data at sea means lower operating power demand. Currently the primary battery charging system is based on solar energy. At high latitudes during the winter months no charging occurs. The application of renewable micro energy resources could possibly extend buoy deployments at high latitudes, charging batteries through low light levels in winter where solar harvesting is not possible. The aim of this paper is to look at the hydrokinetic energy of the wind driven drift current availability during the winter months at high latitudes. By combining the Stokes drift and Ekman surface current a value was calculated for the drift current speed within the top 3 m of the water column and converted to power density. Using the European Medium Range Weather Forecast latest model dataset ERA-5 the annual power density can be plotted at any potential buoy deployment location. The ERA-5 data was validated through comparing it to the locally measured wind speed data recorded by high latitude buoys above 55 degrees North in both the Atlantic and Pacific Oceans. The R^2 values of the comparative data sets are in the range 0.35 to 0.40. This validation also shows that lower wind speeds have a closer correlation, but as wind speed increases the divergence between the observed and the modelled data sets increases. ERA-5 data at two locations at 75^{o}N in the Atlantic basin and 80^{o}N on the Pacific side of the Arctic Ocean was then modelled to provide power density curves at 1 m depth. The results show an increased power density available during the winter months through increased wind speeds more than 5-8 m/s compared with summer months. The increased availability of this wind driven hydrokinetic energy resource during winter months coupled with the ongoing reduction in power demands by oceanic and meteorological data buoys make further research into the development of micro turbines attached to buoys promising.

1. Introduction

Buoy observation platforms and their associated equipment are deployed globally throughout the oceans for purposes such as navigation, hazard marking, and atmospheric and oceanographic data collection that provide vital information for weather forecasting and documenting long-term climate variability. Being positioned typically in remote offshore locations, the equipment on these buoys uses batteries to power their operations and collect and transmit data. Oceanic buoys use a combination of a primary rechargeable battery systems through a solar array and a non-rechargeable modular lithium battery (Venkatesan, et al., 2018). At lower latitudes solar charging all year round provides sufficient and persistent energy for operation of the buoys. However, at higher latitudes, available solar harvesting is limited by the solar angle of incidence and the efficiencies of the solar panels (Hatzianastassiou, et al., 2005) and during winter months there is insufficient sunlight for solar harvesting. For example, at 66^{o} latitude during midwinter daylight can be as little as three hours per day, which is insufficient to power a buoy long term. At 69^{o}, daylight does not occur for 47 days, while at 70^{o} and 80^{o} there is no daylight for approximately 57 days and 120 days, respectively (Burn, 1996; Australian Antartic Program, 2021).

The use of wind turbines mounted for power generation on buoys is not a practical consideration, where the turbines would be susceptible to damage from the waves and freezing temperatures that would impact the blades/turbines through potentially icing over, hence the norm is to use solar panels. Therefore, during winter months at latitudes >66^{o}, these non-rechargeable secondary power system batteries become depleted. This limits the duration of deployment for buoys to be typically one-to-two-year deployments by the non-rechargeable battery availability which is over one winter only (EIVA Marine Energy Solutions, 2016).

In the absence of sufficient solar energy in high-latitude regions, surface ocean currents could be exploited as an energy source for buoys. However, tidal flows in high latitudes in deep water regions are typically small 0.02-0.05m/s (Jenkins & Ekanayake, 2017) and therefore not practical to exploit for their energy (Lewis, et al., 2015, Neill & Hashemi, 2018). But there is a considerable wind energy resource at high latitudes that generates wind-driven surface

currents, as detailed below, that could be exploited for this purpose using surface-mounted tidal-stream turbines. This study, therefore, investigates the feasibility of using wind-driven surface currents as an alternative energy resource for ocean buoys at high latitudes.

There is an estimated 60 TW of downward energy flux through the atmosphere to ocean interface and entering the oceans globally, much of which provides energy for turbulent mixing, baroclinic instabilities of ocean-scale currents such as the Gulfstream, shear stress on the seabed and waves breaking on the shoreline (Thorpe, 2007). Wind stress and its mechanical energy input through the ocean surface is an important component of this energy flux, with an estimated input totalling 3 TW that drives Ekman surface currents, shear surface currents, wave energy and stokes drift (Wantanabe & Hibiya, 2003; Alford, 2003; Wang & Huang, 2004).

The top three meters of the water column has the same heat capacity as the whole of the atmosphere above it (Gill, 1982) and 50% of solar radiation which penetrates the ocean is absorbed within the surface 0.5 m, along with 50% of the kinetic energy from breaking waves being dissipated within 20% of the wave height below the surface (Soloveiv & Lucas, 2013), although orbital motions from the waves continue to a depth of approximately half the wave length of the surface wave (The Open University, 2002). For a surface wave with a 50 m wavelength and 5 m wave height, for example, the size of the surface wave orbital will be 5 m which will decay exponentially to a depth of 25 m at which point the motion will be negligible. Considering this, it is important to understand the energy exchange through this interface. Therefore, the potential availability of wind-driven surface energy is investigated in this study.

A particular challenge is to estimate the input of kinetic energy from the wind to the surface of the ocean through both the surface drag producing a surface current element and wave energy since these processes are in a constant change of flux. To simplify the problem, we can assume an idealised sea state in which there is a constant wind speed and in which waves have become fully developed so that the sea surface roughness in which the energy transfer from wind to water could be defined. In effect when white capping occurs which balances out the energy input from the wind. Wave growth will not increase past this point, this energy

dissipated through white capping provides momentum to the ocean surface increasing the surface current speed. Although due to the fetch and wind speed the sea may not be fully developed (Brown, et al., 2002). Combining the surface drag current element and the wave driven stokes drift component together provides the total wind driven surface current.
Once the wind stops these waves travel as long-distance swell waves losing very little energy (Folley, 2017).

However, the ocean surface elevation is constantly changing through physical processes including tides, turbulence, wind energy input through surface drag, wave motions and energy dissipation through white capping. The wave energy changes as input from the wind or other waves creates a constantly changing wave spectrum as the waves become fully developed. Hasselmann et al (1973) were able to recreate a similar approximation of the wave spectrum, using a fetch limited and constant wind model parameterisation, showing the growth and energy loss. The energy transfer for the wind into surface current depends on the temperature and salinity of the water and therefore its molecular viscosity which affects the wave building and surface drag as the wind blows over the surface creating turbulence (Massel, 1999) dictating the energy transfer from wind to surface currents.

In practice, the energy input into the ocean surface through wind stress (τ) is usually measured as:

$$\tau = \rho_a C_{Da} W_{10}^2 \quad (1)$$

Where the wind speed (W_{10}) is measured at 10 m above mean sea level. The wind stress τ on the ocean surface depends on the magnitude of surface drag coefficient (C_{Da}) and the air density (ρ_a), which in a fully developed sea state can be defined, but not in practice due to the complexities outlined above. Komen et al., (1984) produced an estimate of surface wind stress based on a simple duration limited wind, which proved a good representation of a fully developed sea, for both the wind energy input and included dissipation and nonlinear interactions at the ocean surface.

$$C_{10} = \frac{\mu_*^2}{\mu_{10}^2} = (0.8 + 0.065\mu_{10}) \times 10^{-3} \quad (2)$$

Where C_{10} is the drag coefficient, μ_{10} the wind speed at 10m above mean sea level, and μ_* is the friction velocity or shear stress.

To include these nonlinear interactions requires parameterisation. Hasselmann et al., (1985) provided a parameterisation which is an accurate representation of the nonlinear interactions and is used in the European Centre for Medium Weather Forecasting's Wave Model (WAM), which has been used in this project (see Section 2).

Climate scientists have shown that there has been increasing frequency and intensity of mid-latitude cyclones from the 1950s to the turn of the 20th Century, especially so above 20° latitude in both the northern (Graham & Diaz, 2001) and southern Pacific (Hopkins & Holland, 1997), with increases of up to 40% in the number of strong wind events with wind speeds up to 100 km^{-1}. In turn, higher latitudes have experienced an increase energy input from 0.25 TW in 1950 by up to 0.4 TW by 2000 (Figure 1), with much of this due to increasing sea surface temperatures of $0.11 \pm 0.01^0 C$ per decade from 1975 (IPCC, 2013), that have in turn reduced sea ice extent (e.g. Arctic ocean sea ice has reduced by 2.0% ± 0.2% per decade since 1980 (Cosimo, 2011)).

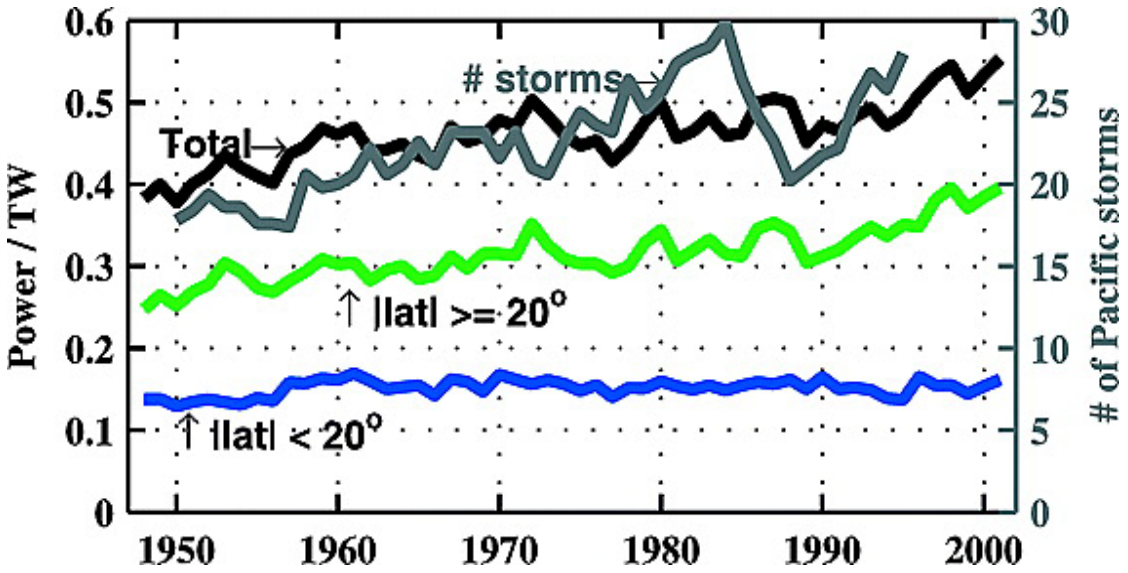

Figure 1. Is the time series from (Graham & Diaz, 2001) from 1948 to 2000 The blue plotting below 20o latitude with energy input flux remaining steady, while the green plot shows the 40% increase at latitudes above 20°. The Black plot is the total flux. The grey line shows the number of pacific storms.

1.1. The surface layer of the Ocean

The wind driven surface current creates a drift current which is generally approximated as 3% of the wind speed at 10 m above the sea surface and reduces to 1.5% at the upper Ekman

layer, which is the layer where there is force balance between the pressure gradient force, turbulence and the Coriolis force, leading to the direction of the drag force causing the surface current in the northern hemisphere to veer 45^{o} from the wind direction. This surface velocity profile can be broken down into three layers. The upper layer extends to a few millimetres', where velocity behaves linearly below the air-sea interface and is dominated by viscosity through changes due to entrained air, pressure, and temperature over water turbulence. Beneath this the mid-layer is a region where current velocity decreases logarithmically from at the surface 3% of the wind speed down to the third layer, the Ekman Layer where the current velocity at its top has decreased to 1.5% of the wind speed (Fernandez, et al., 1996). The surface current finally decreasing to approximately 4% of its surface flow value at a depth of half the wavelength. It is the mid layer below the turbulent surface where the flows will be strongest and practically exploitable by in-stream turbines mounted to buoy deployments. These near the surface currents are comprised of stoke's drift, geostrophic currents, tidal currents, baroclinic currents including those caused by internal waves and direct wind induced currents (Fernandez, et al., 1996). Research by Laxague al., (2018), in the northern Gulf of Mexico was carried out to look at the wind driven near surface currents. Using a combination of near field bamboo plates with a 1.75cm thickness floated on the surface and movement recorded by drone, GPS tracked drifters and acoustic doppler profilers (ADCP) created a current velocity profile in a 13.5 m deep water column. Figure 2 shows the collected results in Table 1 of the drifters and the ADCP data. Their results of the current velocity profile at depth shown in Figure 2, are of higher wind-driven current speeds towards the ocean surface.

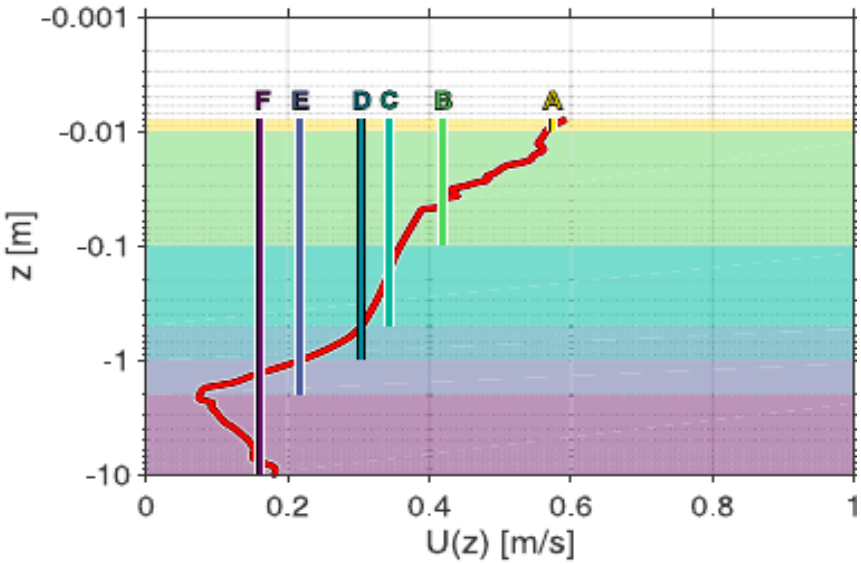

Figure 2. Red line indicates current profile generated from all observational data. the labels A-F marking the coloured layers correspond to the ranges given in table 1. (Laxague, et al., 2018)

Table 1

Comparison of Drift Speeds by Depth Range Averaged by Each Instrument: Drift Speed and Direction. Over Layers of Six Different Thicknesses of the Observed Current Velocity Profile

Segment	Thickness of layer (m)	Measured by	Speed (m/S)	Direction (deg)
A	0.01	Surface tracer	0.57±0.01	242±2
B	0.10	Polymetric camera, drifters	0.43±0.07	250±14
C	0.50	Drifters, ADCP	0.35±0.05	245±13
D	1.00	ADCP	0.30±0.06	231±11
E	2.00	ADCP	0.22±0.10	219±14
F	10.00	ADCP	0.16±0.05	162±40

Note. The error margins given (e.g., 0.57±0.01) represent 1 standard deviation from the mean. The mean wind velocity direction was 242°. Adapted from (Laxague, et al., 2018)

The momentum transfer from the wind blowing over the surface of the ocean is through both shear stress and wave generation making up the total rate at which wind energy input is through the surface. These two components are independent of each other with Stokes drift accounting for two thirds of the wind driven surface current and the wind shear stress the remaining third (Jenkins, 1987; Wu & Liu, 2008; Ardhuin, et al., 2009).

There are three elements currently considered in the wind driven Ekman surface current and the subsurface Ekman layer. These three elements along with a direction component of the observed current drift are discussed below. The last of these the Ekman depth is not relevant to this study.

The Ekman surface current comprises the surface wind stress and direction and the induced surface current. Previous laboratory experiments, observations at sea and models have given a combined surface current approximation of 3% of the wind speed at 10 m above sea mean surface (Pugh, 1987). More recently, the Surface Velocity Programme (SVP) carried out by Chang et al., (2012), used observational data over a period from 1999-2009 where they analysed 14,323 data points from the surface drifters to determine both near surface current drift angles and influence on the surface current at high and low wind speeds. This showed less influence by tidal current on the surface current at wind speeds >20 ms^{-1} but showed a range of surface current drift of between 1.9% - 2.2%. There have also been several HF radar studies; for example, Essen (1993) using a 25-30 MHz radar showed surface drift of between 1.5% -2.5% of the windspeed at 10 m (U_{10}) above mean sea surface. Shay et al (2007) used a 16 MHz radar to measure surface drift with results recoded of 2% - 3% of U_{10}. And finally, Mao & Herron (2008) again using a 30 Mhz radar recorded at surface drift current of >2.1% of U_{10}. These finding show a range of wind generated surface currents from 1.5% - 3% depending on individual studies.

Graham, et al., (2019) conducted a comparison study between data collected by radiosondes released from research vessels which was evaluated against five atmospheric reanalyses models. Two research ship cruises between 25/8/17 – 11/9/17 in the Fram Strait twice daily launched radiosondes at twelve hour intervals to record data at altitudes between 1000hPa to 500hPa recorded atmospheric data, which included wind speed and wind direction. A total of 50 radiosonde recorders were released and compared with modelled data sets. The ERA5 data showing the closest accuracy to the recorded data for wind speed. From the radiosonde's data collected the results for the comparison gave an R value of between 0.88 – 0.94 for the ERA5 wind speed

The Ekman drift surface current (V_E) can be calculated assuming a steady windspeed, constant eddy viscosity of the water, and a rotating Earth. The momentum equation for the surface current is (Stewart, 2008):

$$V_E = \frac{\mathcal{T}}{\sqrt{\rho_w^2 f A_z}} \tag{3}$$

Where, $\mathcal{T}$ is the wind stress, ρ_w^2 water density, eddy viscosity is A_z and f is the coriolis force which is defined as $f = 2\omega sin\varphi$, where ω is the rotation of the Earth at $\omega = 7 \cdot 292 \times 10^{-5} rad\ \mathrm{S}^{-1}$ (Mao & Herron, 2008).

Stokes drift (Us) is the momentum balance of a wave affected Ekman layer current or surface current that includes wave induced Coriolis – Stokes forcing. This is because of the interaction between Stokes drift and planetary vorticity (Hasselman 1970; Xu & Bowen 1994). While Stokes drift is in the wave direction, the Coriolis force affects the path of the water particle, tilting it so that at each revolution it generates movement along the wave. Each of the forces and movements are indicated in the schematic of Figure 3.

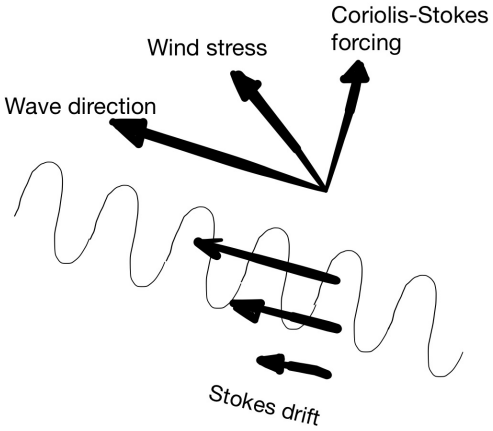

Figure 3. Schematic of the relationship between wind stress, surface wave direction and wave induced Coriolis-Stokes forcing. In the Northern Hemisphere (f<0) adapted from (Hasselmann, 1970)

For a fully developed sea state to occur both the fetch length and wind duration must be sufficient. And a duration of greater than twelve hours wind duration will provide a fully developed sea state. A developed sea state is defined as, one in which waves will not continue to grow, even if the fetch or wind duration increases (Mao & Herron, 2008). This would give a maximum input for Stokes drift.

The Stokes drift (V_s) element of the surface current can be given as (Bye 1967; Xu & Bowen, 1994 Mao & Herron 2008):

$$V_s = \omega a^2 k e^{-2kz} \quad (4)$$

Where, ω is the radian frequency, a the amplitude, k the wave number, and z is the water depth measured from the surface downwards.

The aim of this paper is to characterise, during the winter months in high latitudes, the availability of kinetic energy of the wind drift currents in the upper water column. With a view to identifying the power density created by the current. It is hypothesised the hydrokinetic energy resource of the meteorologically driven surface currents at these higher latitudes make a more persistent and firm renewable energy resource; such a resource could provide a micro renewable energy resource for deployed observation platforms. Here, meteorologically driven currents are assumed to be the combined surface currents of wind induced flow and the wave-induced mean current speed (i.e. Stokes drift), which is hypothesised to be a more persistence renewable energy resource - as driven by two physical processes - further details given in the introduction. Therefore, the objective of this study is to: (a) estimate the combined Stokes drift and direct wind induced surface current values near the ocean surface (between 1 -3 m depth in deep water locations) for several years; (b) analysis the potential resource of this surface current, annual power, and associated variability (including persistence).

2. Methodology

2.1 Data collection

For both Stokes drift and the Ekman surface current a vertical logarithmic profile is assumed and in this model both the wind shear Ekman surface current and Stokes drift are considered as the total effect, making up the wind driven drift current ($\vec{u}drift$). (van der Mheen, et al., 2020). The ERA5 wind and wave data is calculated in this model using equation 5.

$$\vec{u}drift(z) = \vec{u}_0 - \frac{\vec{u}_*}{k}\log\left(\frac{z}{z_0}\right) \quad (5)$$

Where $\vec{u}_0$ is the surface current; with $\vec{u}_* = \sqrt{\frac{\vec{\tau}}{\rho w}}$ the friction current; $\tau = \rho_a C_D \vec{u}_{10}^2$ Is the wind stress; $\vec{u}_{10}$is the wind at ten meters above the surface; C_D is the drag coefficient on the water surface; ρ_w and ρ_a are water and air densities; K =0.41 von Karman's constant; Z_0 the roughness length and z the depth, which is a negative from the water's surface.

The Ekman depth (dE) can be ignored because the study is only looking at the near surface, top two meters. From the surface the Stokes drift decays quickly on a scale that is the Stokes depth (Ds) =L/4. The depth of wave influence for orbital motion is twice the length of the wave. Where at that depth the Stokes, drift is reduced to 4% of its surface value in deep water monochromatic waves (Kinsman, 1965).

In this model the $\vec{u}drift(z)$ in formula (5) provides the combined value of both the Stokes drift and the Ekman surface current. This assumes from the surface of the water column changes in the top couple of millimetres in viscosity through both temperature changes and entrained air can be ignored, concentrating on the second subsurface layer between this and the Ekman layer in which the velocity logarithmically decays with depth ($\log\left(\frac{z}{z_0}\right)$), and having a velocity from the surface downward initially estimated at 3% of the wind speed at U_{10}. The model does not account for any residual velocity in the current but, rather looks at the instantaneous value of the wind speed.

Four high latitude (above 55^{o} N) buoy locations across the Pacific and Atlantic were selected: Wind data for 2020 for the Irminger Sea (59.940N 39.52W) buoy deployed in water depth of 2800m. Wind data for 2017 for the central Bering Sea (57.016N 177.703W) buoy deployed in a water depth of 3687m. Wind data for 2017 the Central Gulf of Alaska (55.883N 142.882W) buoy deployed in a water depth of 3694m. And wind data for 2012 Western Gulf of Alaska (56.232 N 147.949 W) buoy deployed in a water depth of 4054m. The wind data was downloaded from the National Oceanic and Atmospheric administration (NOAA), National buoy data centre, from NOAA's historical quality controlled historical and climatic summaries data their locations are shown in Figure 4 (NOAA, 2021). In line with the study the four buoys selected for the data comparison and validation are all at a latitude above 55^{o}N and were selected as offshore deep-water locations with continuous wind data longer than six months. Wind data was recorded at the buoys using on board anemometers, measuring wind speed at 5 m above the sea surface which is continuously measured and collected every ten minutes. The collected wind speed is for between six and twelve months for different years from these four locations. The data collected has been described in terms of magnitude and variability and used to compare and validate the ERA5 reanalysis wind data, described below.

Figure 4. Validation buoy locations

Global coverage wind data was available from ERA5, provided by The European Medium Range Weather Forecast (ECMWF). This reanalysis model assimilation interpolates global observations and provides amongst other variables: atmospheric precipitation, temperature, wind, wave height and wave period. The ERA5 model data output. From ECMWF, can be downloaded from the Copernicus portal. The ERA5 data outputs are every hour, twenty-four hours a day for a 137 vertical pressure levels from the surface to 80 km above the sea surface. The data grid provided by the ERA5 model is in regular longitude and latitude grids of 0.25^{o} x 0.25^{o} (approximately 31km x 31km) resolution and (European Centre for Medium Range Weather Forecasts, 2019 and Wang, et al., 2019) this available reanalysis data provides global analysis of these data sets from 1979 to present day as hourly reanalysis, highlighting the changes in the Earth's climate and how fast it is changing. The wave model used by ERA-5 is the Wave Model (WAM), which is coupled to an atmospheric wind model. The WAM model in ERA-5 is used in conjunction with the atmospheric component of the integrated Forecasting System (IFS). WAM is a third-generation model and is run as a spherical latitude-longitude grid and can run in any ocean. The model integrates the basic transport equation which describes a two-dimensional ocean wave spectrum from three input functions, the wind energy input, nonlinear energy transfer and a waves dissipation through white capping. WAM predicts the directional wave spectra and its properties which includes wave height, significant wave height, frequency, and swell wave height. (The WAMDI Group, 1988; British Oceanographic Data Centre, 2022). Signficant wave height is an oceanographic term that descirbed the top $1/3^{rd}$ of the, in this case, hourly wave spectra- and therefore described the sea-state for a given location. The swell wave variable was developed to describe bi-modal wave spectra; when there are two distinct wave climates at a location – e.g. swell waves (longer period and lower wave heights due to dispersion relationship) alongside locally generated waves (shorter period and steeper).

2.2 Validation

Wind speed data from the four buoy locations for each buoy was downloaded from the National Oceanic and Atmospheric Administration's (NOAA) National Data Buoy Centre data bases (NOAA, 2021). The ERA-5 data for the same location and time was downloaded from the ECMWF Copernicus data base (The European Medium Range Weather Forecast, 2021).

This validation is expected to have small variations and random errors because the buoy data is collected by anemometers which are typically five meters above mean sea level (AMSL) on this type of buoy when the buoy is vertical in the water, the ERA5 reanalysis data is calculated at 10m AMSL. Also, with a tethered buoy as the wind speed increases the buoy is pushed downwind and the angle at which the buoy is lying in the water will not be perpendicular to the water surface, because as the catenary curve in the anchor cable straightens and the buoy leans over causing using the anemometer rotation to come out of horizontal potentially causing reading errors while also lowering anemometer height. The windspeed measurements between the two heights also creates a small change in the surface friction velocity (μ_*) with $\mu_5 \approx 0 \cdot 94\mu_{10}$ (Komen, et al., 1984).

2.3. Analysis methods. Conversion to flow and power

The ERA-5 wind data was first converted to a current flow speed at three one-meter intervals to a three meter depth below the surface using

$$uzW = Wx0.03 - \left(BETA \times \log\left(\frac{z}{z0}\right)\right) \quad (6)$$

Where the surface z0=0.001, BETA = 0.0027, W = wind speed and z = depth below the surface. The ERA-5 significant wave height data was downloaded as part of the data set a enable the calculated to give Stokes drift element of the surface current to be calculated using equation (7) and then both were added together to provide a surface current value at the three depths.

$$Stokes\ drift = \omega \times k \times ((\frac{H_s}{2})^2) \times \exp(2 \times k \times -1) \quad (7)$$

Where $\omega = \frac{2\pi}{T}$, k is the wave number, and H_s is wave height.

Wind-driven surface flows

The graph in Figure 5 shows the current speed at depths of 1 -3 meters below the surface referenced to the measured wind speed calculated using formula (6). The envisaged micro energy turbine attached to the buoy would be at a depth of between one to three meters, the higher in the water column the greater the resource.

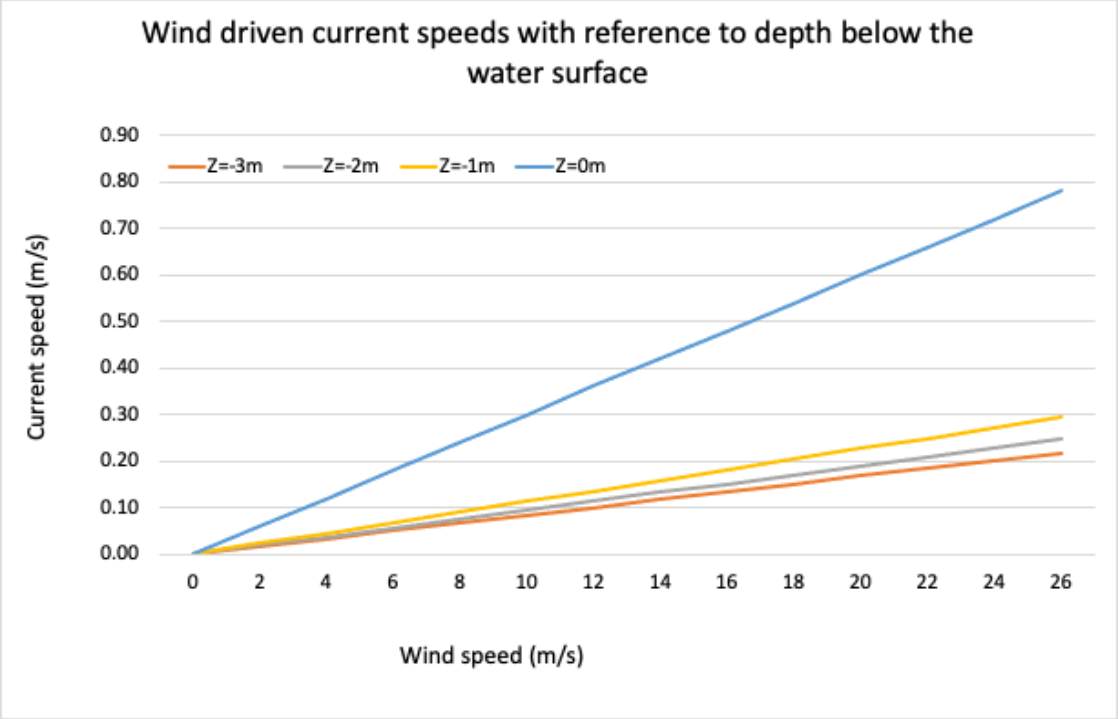

Figure 5. Wind driven current combined Ekman surface current and stokes drift using formula (6) shows the current speeds at depths 0 - 3 meters from the surface.

The power density at the three one-meter depths was calculated from the output of (6) and (7) using Power / Area equation.

$$P/A = 0.5 \times \rho \times U^3 \quad (8)$$

Where ρ = 1025 kg/m3 and U m/s is the surface current driven by wind at 10m and the Stokes drift.

2.4 High latitude data point locations

As a final step, the above procedure can be applied to locations without buoys. Two locations are selected to plot from the ERA-5 data at high latitudes shown in Figure 6, where no buoys are currently. Data set 1 on the Pacific Ocean side at 80°N and data set 2 at 75° on the Atlantic Ocean side. The results of the resource availability as individual elements and a total wind driven surface current including monthly averaged power density curves for the two locations are shown below in Figures 7 – 10.

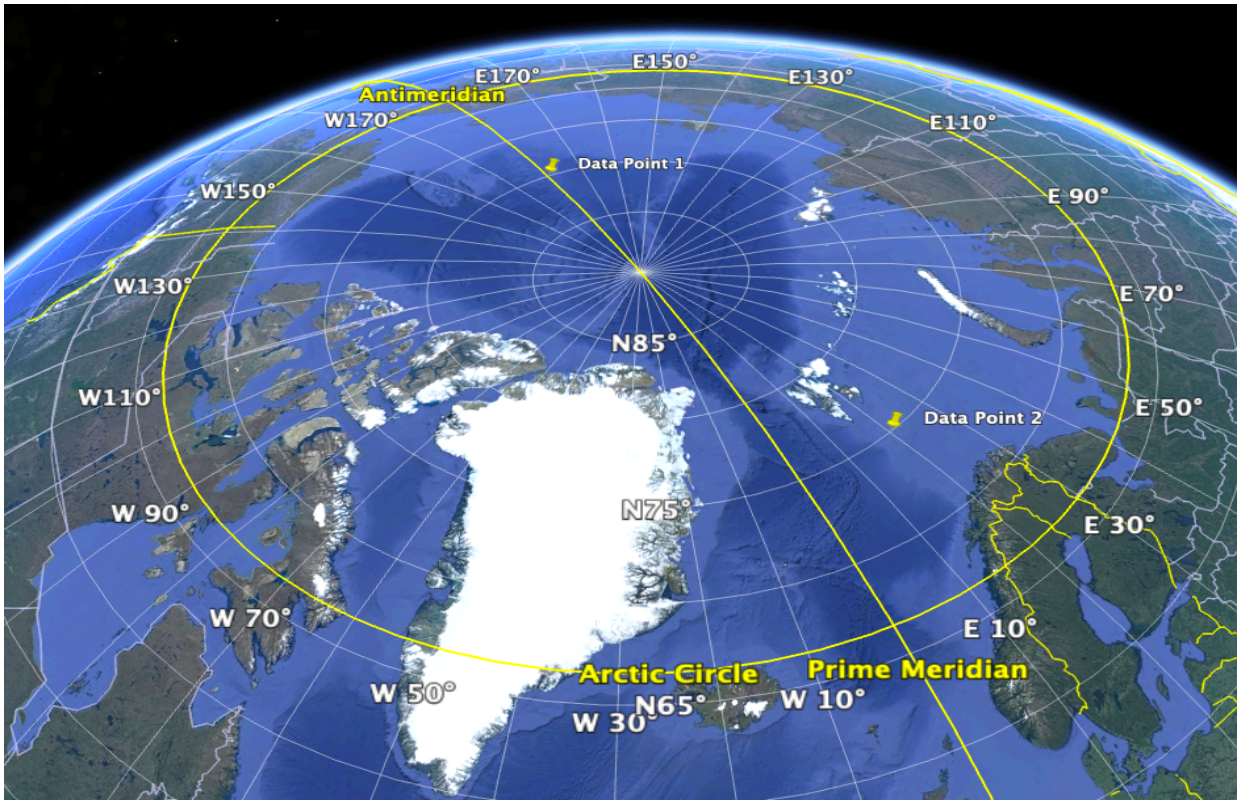

Figure 6. ERA-5 data set locations for plotting the Power density at high latitudes. Data set 1 at 80^{o} N and with data set 2 at 70^{o} N latitudes

3. Results

3.1. Observational and ERA-5 wind data

Plotting the windspeed data in the Annex Figures 11 -14 shows variability in wind speed in both the collected buoy data and the ERA-5 data. Both data sets for each buoy plotted as wind speed against time and have similar profiles.

The amplitude of the wind speed data is slightly higher in all ERA-5 data sets than that of the buoy collected windspeed data. With both showing a seasonal trend of increased wind speed during the important winter months when the resource would be required. The annual Pacific Ocean plots in the Bering Sea and the Gulf of Alaska show an overall increase in wind speeds of up to 5-6 m/s and higher wind speed events during the winter months, with wind speeds increasing from summer highs of typically 15m/s up to 23 - 24 m/s. These four sets of plotted data are included in the Annex Figures 11-14. The four sets of plots below show data from each of the four locations showing in each panel A the data collected by the buoy and the panel B showing the same location and period produced by the ECWMF's ERA-5 reanalysis data. The first plots, in Annex Figure 11 shows a year's wind speed data collected from a weather buoy in the central Bering Sea in panel A while in panel B at the same location and period is shown the ERA-5 data. All four wind plots are very similar in pattern displayed at the four locations with the other three shown in Annex Figures 12, 13 & 14. Most noticeable in both sets of data is that during the winter months the peaks in wind speed are higher than during the summer months typically 5 – 6 m/s but with some winter peaks more the 10 m/s higher.

Annex Figure 12 shows the wind speed for both data sets from the Western Gulf of Alaska with higher wind speeds during the winter months. Annex Figure 13 shows the wind speed for a buoy and the reanalasys ERA5 data in the Central Gulf of Alaska and finally. Annex Figure 14 shows both the buoy and the ERA5 windspeed data in the Irminger sea off Greenland spanning the winter months, quarter 4 of 2020 and quarter 1 of 2021.

3.2. Validation

The scatter plots in the Annex figures 15 - 18 show the buoy observed wind speed versus the ERA5 data. The overall comparison of observed wind speed to ERA5 wind speed at four locations, is given in Table 2 as R^2 values. The R^2 value descirbes the linear regression between the observed (x) and the ERA5 predicted (y) throughout the whole record. Differences between the observed and modeled (scatter of data in Figures 15, 17-18) are likely due to sub-scale and unresolved processes in the model, including natural varibility; whilst the slight difference in buoy location and the model output location (latitude/longitude) as well as vertically (5m and 10m – however no interpolation was performed as the buoy will be moving with tide-surge and waves) will also added to a lower R^2 value. There appears to also be a trend in the model accuracy with wind speed (x) in Figures 15-18; as the data points at very high wind speed values typically appear above the mean trend line – but are likely due to sea surface roughness parameterisation in the model (the ERA5 model has a time-varying sea surface roughness parameter to account for wave growth impact to wind speed: see https://confluence.ecmwf.int/display/CKB/ERA5%3A+data+documentation/). The over-estimation of the ERA5 wind speed at these higher wind speeds therefore suggests the wave-induced slowing of the 10m wind speed is not well-acounted for in the ERA5 data; and future work could investigate the sea-state driven impact to ERA5 accuracy (including seasonal differences), but is not the objective of this thesis.

Table 2. Values of R^2 showing proportion of variance between the buoy and ERA-5 values and the difference between the quarterly averaged values of the two. The negative values are where the buoy data is less than the ERA5.

Buoy Name / Location	R^2 value	Quarterly windspeed difference between the buoy and ERA5 data			
		Q1	Q2	Q3	Q4
Central Bering sea	0.4	-0.3	0.2	0.2	1.1
Western Gulf of Alaska	0.35	-0.7	-0.6	0.6	0.1
Central Gulf of Alsaka	0.47	0.7	0.3	0.3	-0.1
Irminger sea in the Labrador Basin	0.36	-0.8			-0.2

Which with the previously discussed differences in height reference and other collection errors can explain some of the variance.

With these large data sets plotted in each of the locations, three of which are annual data sets measurement taken hourly and in excess of eight thousand data points per set. The plot of the Irminger sea is for the two quarters with measurements take every ten minutes has over seventeen thousand data points. Small amounts of variation in these data sets because of the number of data points can quickly reduce the R^2 value. There is greater variance at the higher wind speeds and with the large data sets the larger windspeed difference will reduce the correlation coeffient. This is highlightled by the divergance of the orange trend line from the black 1-1 reference line, the higher the wind speed the greater the divergance.

3.3. Power

3.3.1. Power resource for sites 1 and 2

The time series for the 2020 power resource at both sites 1 and 2 at one meter depth is shown in Figure 7. Panel (a) shows the wind speed and power per square meter in the air at the two sites which is highly variable and, in our model, is an instantaneious value and has no memory (momentum). Panel (b) showing the wave power from Stokes drift, is less variable and has wave memory with the large waves are primarily during the winter months. As can be seen these do not necessarily fall to a zero value unlike the wind, providing a persistant current even with the wind variations. The combined wind and wave current is shown in panel (c) because the current is the combined wave power and wind driven surface current, the resource is magnified also the intermittency is created by the wind persistence i.e. the persistence of the current is a combination of the wind and the waves.

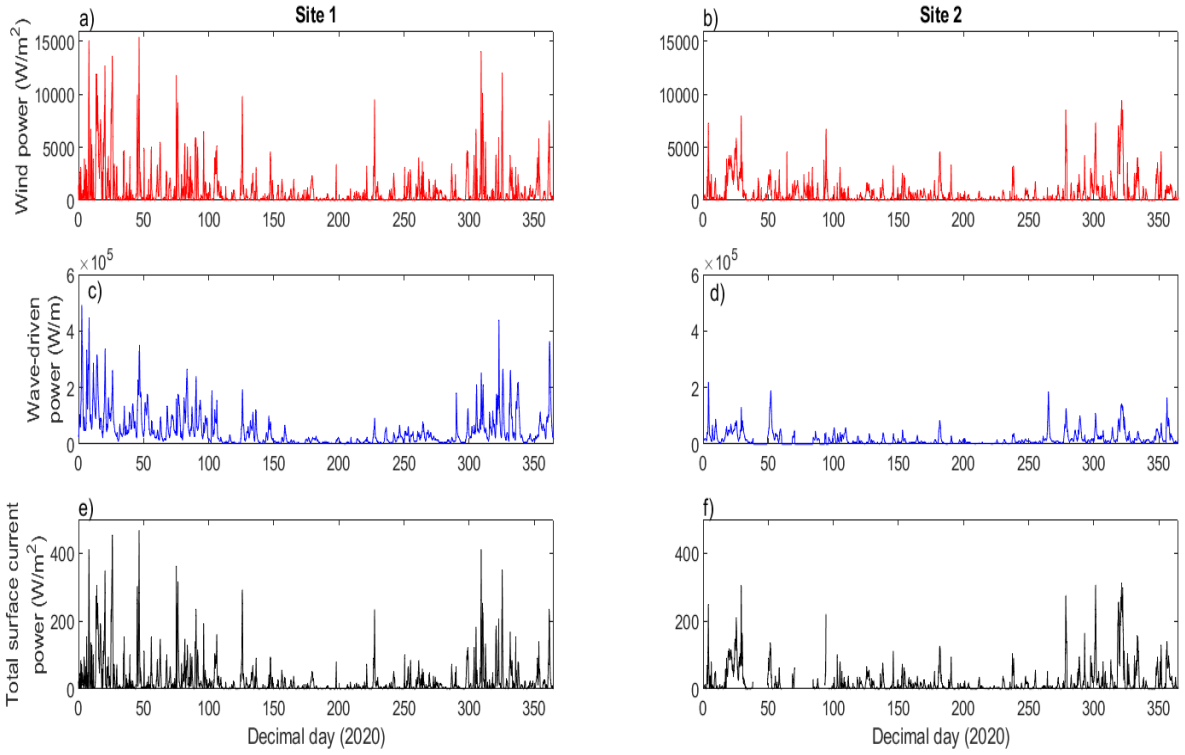

Figure 7. Time series of the wind power (a), Stokes drift (b) and wind driven ocean current power (c) at 1 meter depth of sites 1 & 2 for 2020.

Figure 8 shows the probability of exceedance giving the availability of each component panels a & b, wind driven surface current power; c & d, the wave driven power; and e & f, the combined wind driven surface and wave driven current.

As can be seen in Figure 7, the persistence of the current as a resource is higher because it is the result of combined wind and wave climates; as such the persistence of currents is higher even though there were times of low wind, but a wave resource (or vice versa) and can be seen in Figure 8 as divergence of the normalised resource between wind, wave and current. The wave resource being largest for more than 60% of the year with the combined current the remaining 40% of the year.

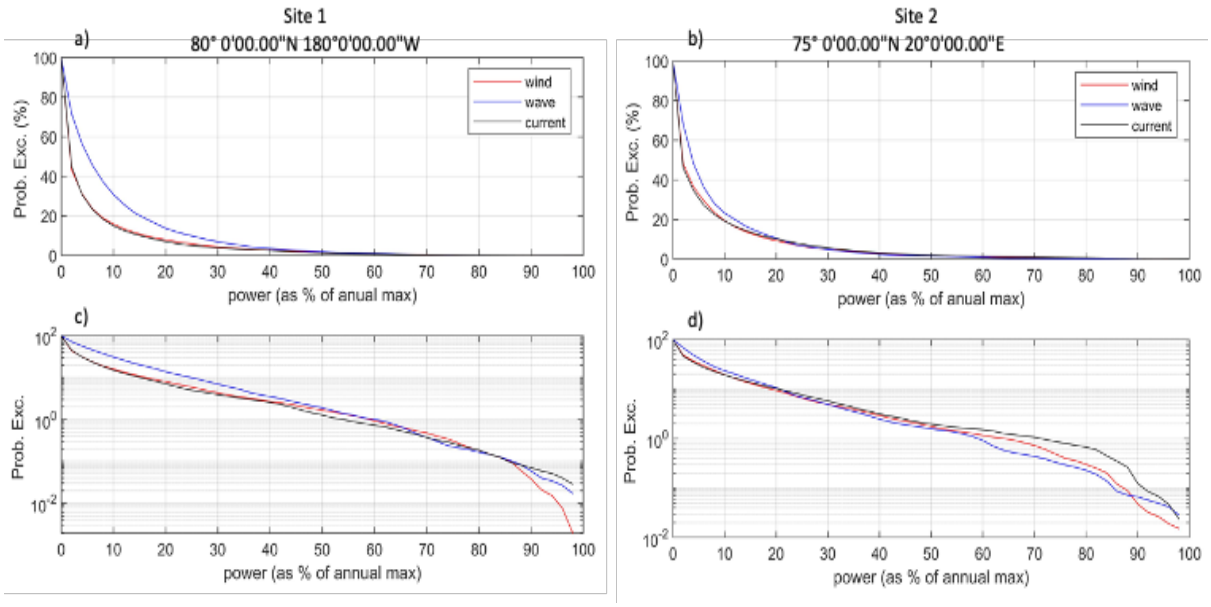

Figure 8. Probability of exceedance graphs for sites 1 & 2 showing the wind and wave availability and the combined availability for the wind driven surface current for 2020.

3.3.2. Averaged monthly power values

Figures 9 and 10 shows the available power density at 1 meter below the surface generated by the wind through the Ekman surface current and Stokes drift, averaged per month over the year at both locations. At a latitude of 75° North the sun does not rise above the horizon approximately 95 days from the 5th of November to 7th of February. This increases to at 80° North during which winter darkness lasts for 122 days typically 22nd of October to 20th of February (Burn, 1996). Both figures show that the period of increased wind speed and of highest average power density is during the winter months. The night-time / twilight periods shown in the grey shaded area.

At these two location points during the periods of winter darkness the average power available of the two sites shown in Figures 9 and 10, is that at site one 42.26 W/m^2 and at site two 29.41 W/m^2 at 1 meter below the surface. In figure 7 for the both points 1 and 2 the combined surface current is greater during these winter months.

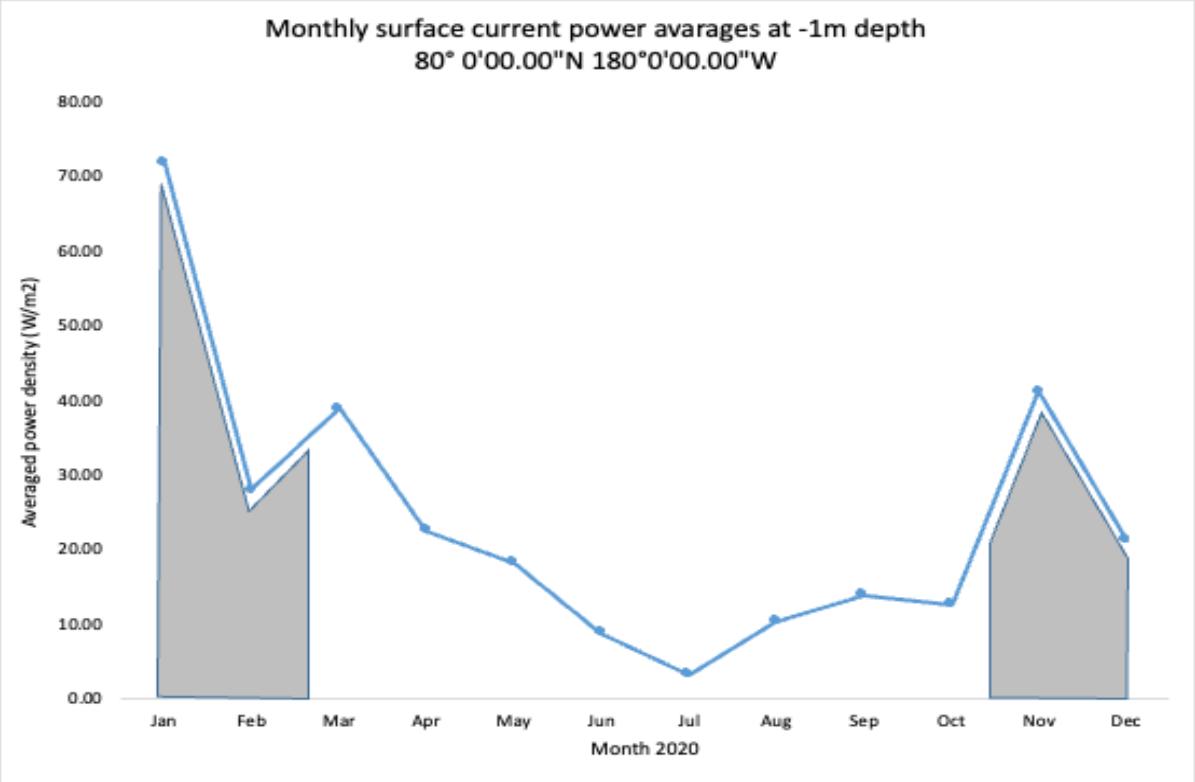

Figure 9. Data point 1. Monthly averaged power density graph at 80^0N along the Anti Meridian. Showing periods of darkness during the winter hatched in grey

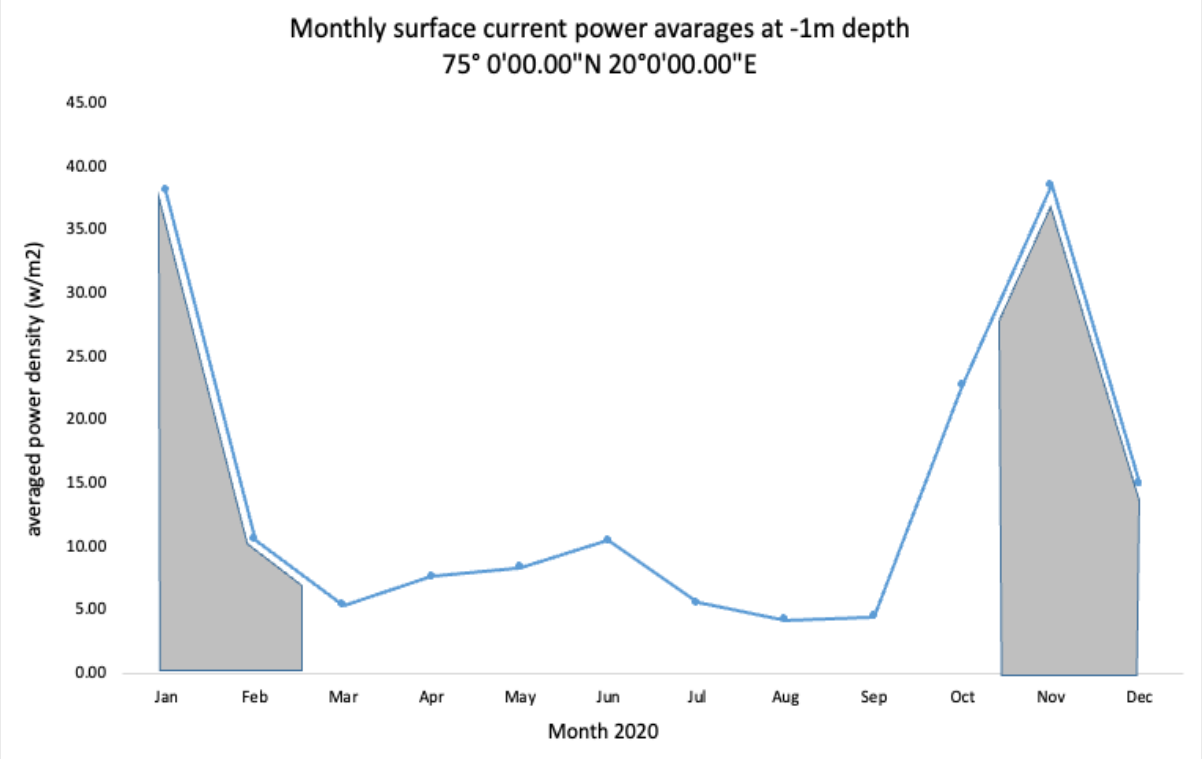

Figure 10. Data Point 2. Monthly averaged power density graph at 75^0N, 20^0E. Showing periods of darkness during the winter hatched in grey.

4. Discussion and conclusion

4.1 Summary

The proof-of-concept results from this study suggest that: (1) there is potentially a sufficient resource of sea surface energy flux at high latitudes for the purpose of exploiting as a renewable energy resource for powering buoys, via instream turbines; and (2) the global reanalysis data ERA 5 is appropriate for estimating the resource spatially. However, our evaluation suggests that resource estimates using ERA 5 data should be performed over seasonal timescales. ERA 5 data for multiple decades from 1979 - 2022 is available as hourly reanalysis data for any location. The comparison of the collected wind speed data from the buoy locations and the ERA 5 reanalysis (annex Figures 9 – 12) showed similar seasonal variation but with large differences over smaller timescales (e.g., hours-to-days). Results in the regression analysis show an R^2 value of between 0.35 – 0.47, the regression lines in the annex Figures 13 - 16 show greater alignment at the lower wind speeds, while diverging as wind speeds increase. Some of this is certainly due to the differences in data collection with the buoy wind speed being collected at 5 m and ERA 5 data at 10 m above sea level.

Maximum power availability occurred during the winter months. This was shown via the buoy wind data and corresponding power density calculations, and by applying the ERA-5 wind data/power calculations to two locations on opposite sides of the Arctic Ocean at 75^0 and 80^0N (close to the Prime Meridian and the Antemeridian) (Figures 7 & 8). The average power for each the two data point locations is 42.26 W/m^2 and 29.41 W/m^2. The winter months coincide with periods of darkness and low light levels before the start and end of winter, and hence when an alternative (to solar) energy source would be needed. Although this pattern of increased wind speed and increased power density during the winter is ideal, site-specific and technology-specific estimates that cover seasonal and interannual variability are required to assess whether the resource is sufficient to supply a micro energy resource.

4.2 **Assumptions / limitations / uncertainties**

There are several uncertainties, limitations and assumptions made in the calculation of the power density. The ERA 5 reanalysis data has less data points for references at high latitudes as opposed to the more populous and areas with regular shipping routes. Given the cascade of uncertainties of ERA5 resolved wind speed, and unresolved processes/errors in the estimated current speed, the hydrokinetic resource resolved will contain uncertainties; however I do not aim to resolve the actual resource (i.e. annual yield estimate) but instead highlight the firm and persistent resource the weather-driven ocean surface current could provide compared to other renewable resources (e.g. solar-PV) or single resources (e.g. just wave energy devices) because of the combination of wave and wind induced surface currents. Therefore, uncertainties in the resource, such as possible effects of taking into account 3% rather than 1.5 -3%, will impact the instantaneous power but not the resource climate (i.e., gaps in potential power conversion) or the probability exceedance plots of Figures 8-10 (e.g., the y-axis values of Figures 9-10 should be improved in future work, but the shape of the blue line is unlikely to change).

4.3 **Power conversion inefficiency**

Direction of the wind driven current flow is variable. With this variation helical turbines would probably be the preferred option to integrate into buoys. Field tests carried out by Zhang, et al., (2022) on small 0.45m high helical bladed turbines at current speeds of between 1.2m/s upto 3.5m/s showed a turbine device efficiency (Cp) of 0.19 to 0.20. which is promising for these low wind driven current speed values. This power conversion rate is comparable with solar efficiency (Hatzianastassiou, et al., 2005).

4.4 **Conclusion**

In this paper we have discussed the effect of wind driven surface current in the upper three meters of the water column and its availability to provide a micro energy resource especially for high latitude energy harvesting during the winter months when solar charging is unavailable. Further, we have identified that the ERA-5 data can be used to provide a

historical multiyear power density for any location assisting in possible future buoy deployment locations and their potential micro energy resource. Deployment of more data collection buoys at high latitudes for longer periods without recovery could assist in monitoring changes in the Arctic. Several wind farm development zones / study areas in the Norwegian and Barents Seas have been identified (4C OffShore, 2022) in which data and marker buoys would be required.

The temperature increase in the Arctic since the 1970s is almost 2^{o}C (Pistone, et al., 2014) and with summer mixed layer temperatures in the Arctic basin rising at 0.5^{o}C per decade since 1982 (Timmermans, et al., 2017) climate sea surface temperatures continue to rise, depletion of sea ice currently at levels of 11% ± 0.132% per decade will continue in all regions in the Arctic >60^{0}N (Cosimo, 2011; Cosimo, et al., 2017) and by the end of the century may lead to higher latitudes becoming ice free during the summer months up to the end of September if the temperatures rise by 2^{o}C above preindustrial levels (Mahlstein & Knutti, 2012; Jahn, 2018).

Future research could be identifying the power requirement winter needs of various observation platform equipment types. Also modelling helical blade turbines at these very low flow rates to fully understand if they could work and if so the height and diameter of the turbine assembly to produce the required power.

References

4C OffShore, 2022. *Global ofshore wind farm database.* [Online]
Available at:
https://map.4coffshore.com/offshorewind/index.aspx?lat=70.943&lon=22.551&wfid=NO31
[Accessed 28 May 2022].

Alford, M. H., 2003. Improved global maps and 54-year history of wind-work on ocean inertial motions. *Geophysical Research Letters,* 30(8).

Ardhuin, F. et al., 2009. Observation and Estimation of Lagrangian, Stokes, and Eulerian Currents Induced by Wind and Waves at the Sea Surface. *Journal of Physical Oceanography ,* Volume 39, pp. 2820-2838.

Australian Antartic Program, 2021. *How much daylight is there in Antarctica during summer and winter?.* [Online]

Available at: https://www.antarctica.gov.au/about-antarctica/weather-and-climate/weather/sunlight-hours/ [Accessed 17 November 2021].

British Oceanographic Data Centre, 2022. *Wave Modelling (WAM).* [Online]
Available at: https://www.bodc.ac.uk/data/documents/nodb/254628/ [Accessed 4 October 2022].

Brown, E. et al., 2002. Waves. In: *Waves, Tides and Shallow water processes.* Milton Keynes: The Open University, pp. 15 -16.

Burn, C., 1996. *The Polar Night,* Yukon: Artisan Press Ltd.
Chang, Y. C. et al., 2012. Observed near-surface currents under high wind speeds. *Journal of Geophysical Research,* Volume 117, pp. 1-6.

Cosimo, J. C., 2011. Large Decadal Decline of the Arctic Multiyear Ice Cover. *Jounrnal of climate,* 25(1176-1193).

Cosimo, J. C., Meier, W. N. & Gersten, R., 2017. Variability and trends in the Arctic Sea ice cover: Results from different techniques. *Journal of Geophysical Research:Oceans,* Volume 122, pp. 6883-6900.

EIVA Marine Energy Solutions, 2016. *https://www.eiva.com/about/eiva-log/how-an-intelligent-power-handling-system-will-increase-the-lifespan-of-a-data-buoys-power-system.* [Online] b[Accessed 17 March 2022].

European Centre for Medium Range Weather Forecasts, 2019. *Global reanalaysis: Goodbye ERA Interim.* [Online]
Available at: https://www.ecmwf.int/en/newsletter/159/meteorology/global-reanalysis-goodbye-era-interim-hello-era5 [Accessed 21 February 2020].

Fernandez, D. M., Versecky, J. F. & Teague, C. C., 1996. Measurements of upper ocean surface current shear with high-frequency radar. *Journal of Geophysical Research,* 101(C12), pp. 615-625.
Folley, M., 2017. The Wave Energy Resource. In: *Handbook of Ocean Wave Energy. Ocean Engineering & Oceanography.* s.l.:Springer, pp. 43-47.
Gill, A. E., 1982. Atmosphere-Ocean dynamics. In: s.l.:Cambridge University Press, pp. 662-663.
Google, 2021. *Google Earth.* [Online]
Available at: https://earth.google.com/web/@73.51149459,-108.03177355,-5183.25335342a,9358662.69314647d,35y,0h,0t,0r [Accessed 15 December 2021].

Graham, N. E. & Diaz, H. F., 2001. Evidence for Intensification of North Pacific Winter Cyclones since 1948. *Bulletin of the American Meteoroligical Society,* Volume 82, pp. 1869-1893.

Graham, R. M., Hudson, S. R. & Maturilli, M., 2019. Improved Performance of ERA5 in Arctic Gateway Relative to Four Global Atmospheric Reanalyses. *Geophysical Research Letters,* Volume 46, pp. 6138-6147.

Hasselmann, K., 1970. Wave-Driven Inertial Oscillations. *Gyophysical Fluid Dynamics,* Volume 1, pp. 463-502.

Hatzianastassiou, N. et al., 2005. Global distribution of the Earth's surface shortwave radiation budget. *Atmospheric Cheistry and Physics,* Volume 5, pp. 2847-2867.

Hopkins, L. C. & Holland, G. J., 1997. Australian Heavy-Rain Days and Associated East Coast Cyclones: 1958–92. *American Meteorolgical Society,* Volume 10, pp. 621-635.

IPCC, 2013. *Intergovernmental Panel on Climate Change,* Cambridge, UK: Cambridge University Press.

Jahn, A., 2018. Reduced probability of ice-free summers for 1.5 °C compared to 2 °C warming.. *Nature climate Change,* 8(5), pp. 409-413.

Jenkins, A. D., 1987. Wind and Wave Induced Currents in a Rotating Sea with Depth-varying Edd Viscosity. *Journal of Physical Oceanography,* Volume 17, pp. 938-951.

Jenkins, N. & Ekanayake, J., 2017. 7.2. Tidal Stream Resource. In: *Renewable Energy Enginering.* Cambridge: Cambridge university Press, pp. 242-243.

Komen, G. J., Hasselmann, S. & Hasselmann, K., 1984. On the Existence of a Fully Developed Wind-Sea Spectrum. *Journal of Physical Oceanography,* 14(8), pp. 1271-1285.

Laxague, N. J. et al., 2018. Observations of Near-Surface Current Shear HelpDescribe Oceanic Oil and Plastic Transport. *Geophysical Research letters,* Issue 45, pp. 245-249.

Lewis, M., Neill, S. P., Robins, P. E. & Hashemi, M. R., 2015. Resource assessment for future generations of tidal-stream energy arrays. *Energy,* Volume 83, pp. 403-415.

Mahlstein, I. & Knutti, R., 2012. September Arctic sea ice predicted to disappear near 2°C global warming above present. *Journal of Geophysical Research: Atmospheres,* 117(D6), p. http://dx.doi.org/10.1029/2011JD016709.

Mao, Y. & Herron, M. L., 2008. The Influence of Fetch on the Response of Surface Currents to Wind Studied by HF Ocean Surface Radar. *Journal of Physical Oceanography,* Volume 38, pp. 1107-1128.

Markus, T., Stroeve, J. C. & Miller, J., 2009. Recent changes in Arctic sea ice melt onset, freezeup, and melt season length. *Journal of Physical Research ,* Volume 114, p. C12024.

Massel, S. R., 1999. Physical and Chemical Properties of Sea Water, & Wind- Wind driven Surface & Near-Surface Currents. In: *Fluid Mechanics for Marine Ecologists.* Berlin Heidelberg: Springer, pp. 8-9 & 214-216.

National Oceanic and Atmospheric Administration, 2019. *Data Access.* [Online] Available at: http://www.aoml.noaa.gov/phod/floridacurrent/data_access.php [Accessed 4 January 2019].

Neill, S. P. & Hashemi, M. R., 2018. Other Forms of Ocean Energy. In: *Fundamentals of Ocean Renewable Energy.* London: Elsevier Ltd, pp. 141-145.

NOAA, 2021. *National Buoy Data Center.* [Online] Available at: https://www.ndbc.noaa.gov [Accessed 20 January 2022].

Pistone, K., Eisenman, I. & Ramanathan, V., 2014. Observational determination of albedo decrease caused by vanishing Arctic sea ice. *Proceedings of hte National Academy of Siences,* Volume 9, pp. 3322-3326.

Pugh, D., 1987. Current Profiles. In: *Tides, Surges and Mean Sea-level.* Avon: John Wiley & Sons Ltd, pp. 199-200.

Soloveiv, A. & Lucas, R., 2013. The Ocean Near-Surface Layer in the Ocean-Atmosphere system. In: Springer, ed. *The Near-Surface Layer of the Ocean: Structure, Dynamics and Applications.* 2nd Edition ed. s.l.:Springer Science & Business Media, p. 1.

Stewart, R., 2008. Wind driven ocean circulation. In: *Introduction to physical oceanography.* s.l.:Open Source, pp. 205-210.

The European Medium Range Weather Forecast, 2021. *ERA5 hourly data on single levels from 1979 to present.* [Online] Available at: https://cds.climate.copernicus.eu/cdsapp#!/dataset/reanalysis-era5-single-levels?tab=form [Accessed 24 June 2021].

The Open University, 2002. Chapter 1. Waves. In: G. Bearman, ed. *Waves, Tides and Shallow water processes.* Milton Keynes: Butterworth Heinemann, pp. 20-21.

The WAMDI Group, 1988. The WAM model - A Third Generation Ocean Wave Prediction Model. *Journal of Physical Oceanography,* Volume 18, pp. 175-1810.

Thorpe, S. E., 2007. *An introduction to Ocean Turbulence.* Ist Edition ed. Cambridge: Cambridge University Press.

Timmermans, M. L., Ladd, C. & Wood, K., 2017. *Arctic Report Card: Update for 2017.* [Online] Available at: https://arctic.noaa.gov/Report-Card/Report-Card-2017/ArtMID/7798/ArticleID/698/Sea-Surface-Temperature [Accessed 28 May 2022].

van der Mheen, M., Pattiaratchi, C., Cosoli, S. & Wandres, M., 2020. Depth-Dependent Correction for Wind-Driven Drift Current in Particle Tracking Applications. *Frontiers in Marine Science,* Volume 7.

Venkatesan, R. et al., 2018. Best Practices for the Ocean Moored Observatories. *Frontiers in Marine Science,* Volume 5.

Wang, C. et al., 2019. Comparison of ERA5 and ERA-Interim near-surface air temperature, snowfall and precipitation over Arctic sea ice: effects on sea ice thermodynamics and evolution. *The Cryosphere,* Volume 13, pp. 1661-1679.

Wang, W. & Huang, R. X., 2004. Wind Energy Input to the Ekman Layer. *Journal of Physical Oceanography,* Volume 34, pp. 1267-1275.

Watanabe, M. & Hibiya, T., 2002. Global estimates of the windinduced energy flux to inertial motion in the surface mixed layer. *Geophysical Research Letters,* 29(8).

Woodgate, R. A., Weingartner, T. & Lindsey, R., 2007. The 2007 Bering Strait oceanic heat flux and anomalous Arctic sea-ice retreat. *Geophysical Research Letters,* 37(1), p. L01602.

Xu, Z. & Bowen, A. J., 1994. Wave and Wind-Driven Flow in Water of Finite Depth. *Journal of Physical Oceanography,* Volume 24, pp. 1850-1866.

Zhang, A. et al., 2022. Field tests on model efficiency of twin vertical axis helical hydrokinetic turbines. *Energy,* 247(https://doi.org/10.1016/j.energy.2022.123376).

Annex of additional figures

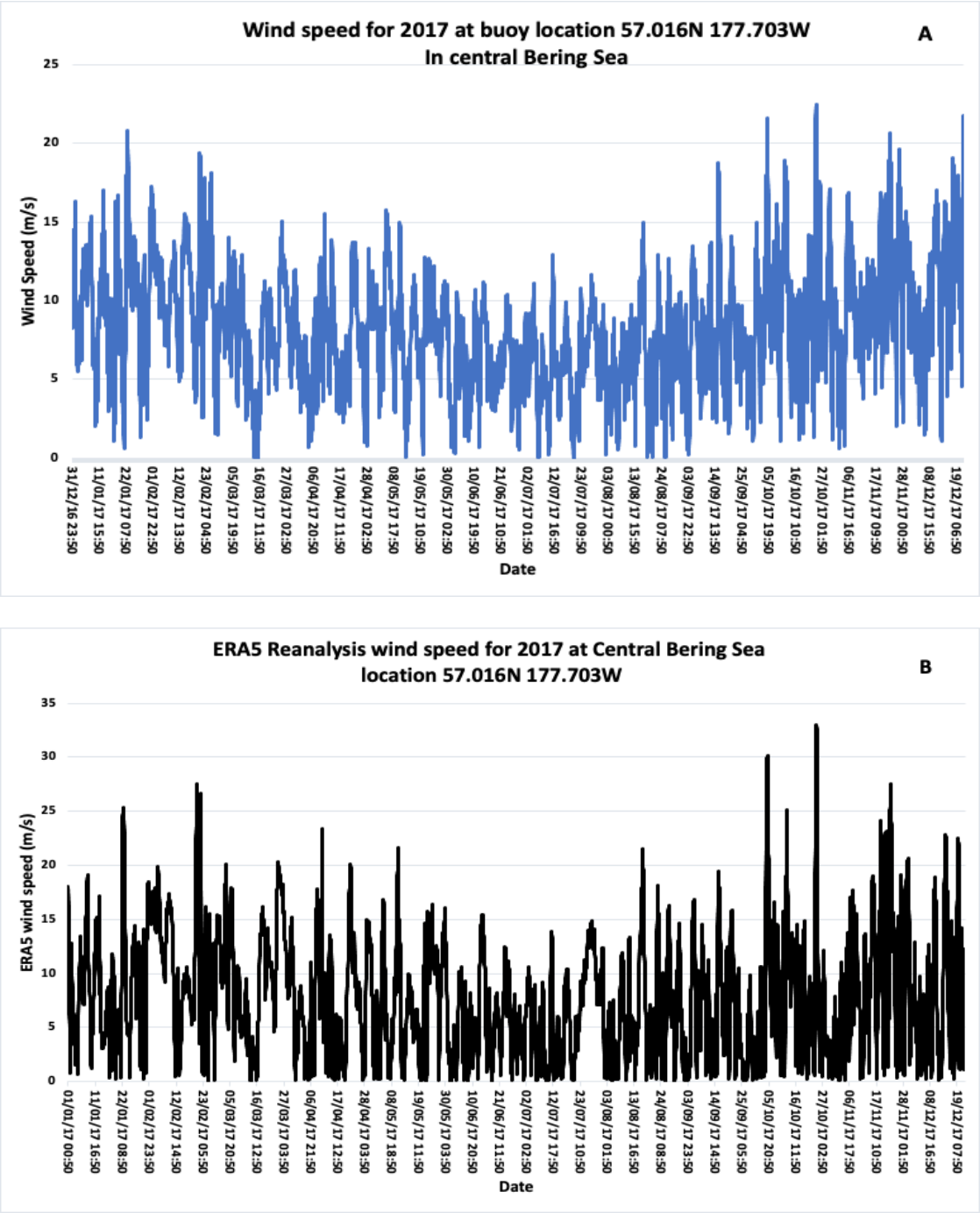

Figure 11. Panel A 2017 annual wind data collected by NOAA weather buoy for 2017. The wind data plotted is every 10 minutes. The buoy from which the data was gathered has an overall height including the anemometers of five meters. (NOAA, 2021) Panel B is the ERA5 reanalysis data for the same grid reference and period.

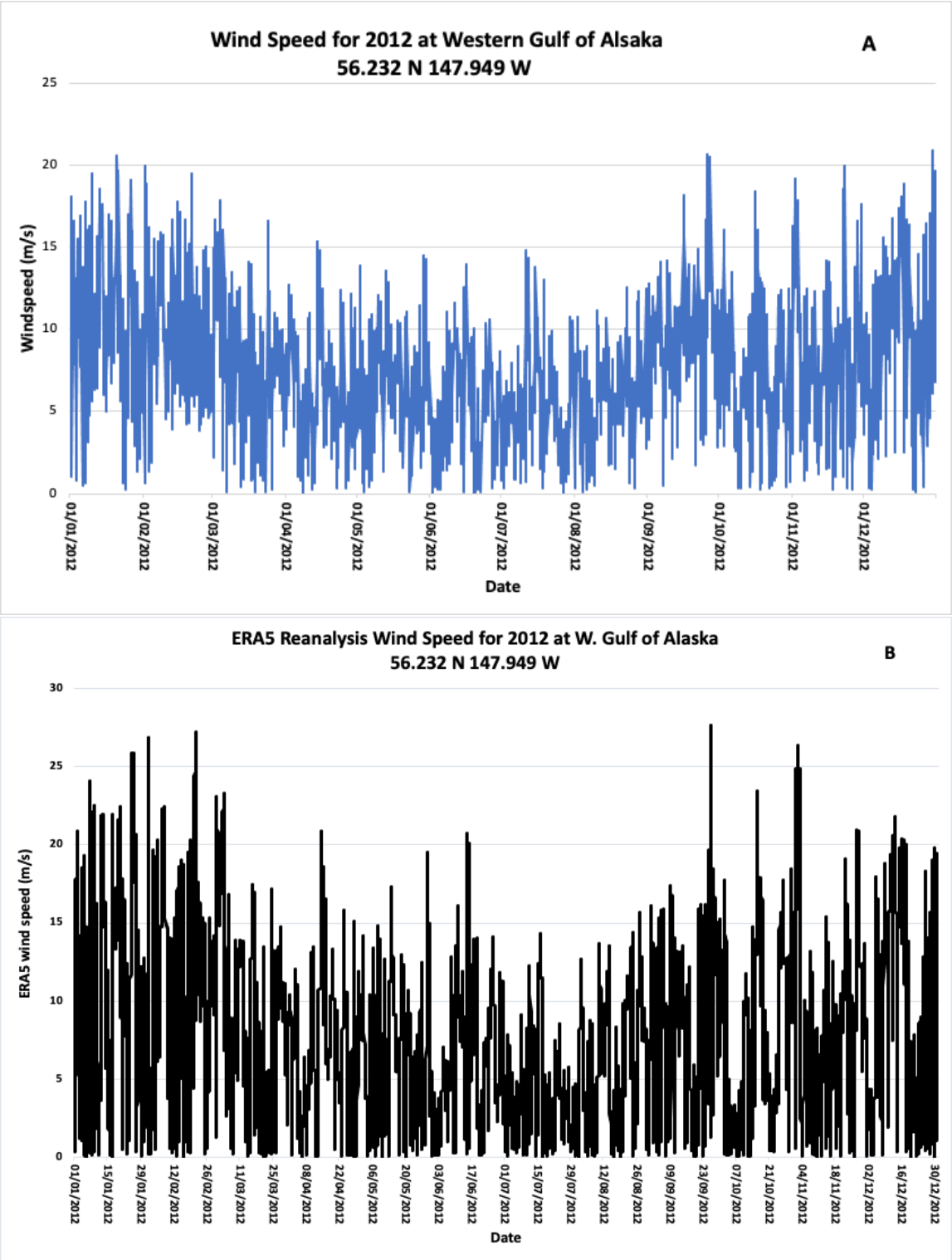

Figure 12. Panel A 2012 wind data collected by NOAA weather buoy for 2012. The wind data plotted is every 10 minutes for the entire year. The buoy from which the data was gathered has an overall height including the anemometers of five meters (NOAA, 2021) Panel B is the ERA5 reanalysis data for the same period and grid reference

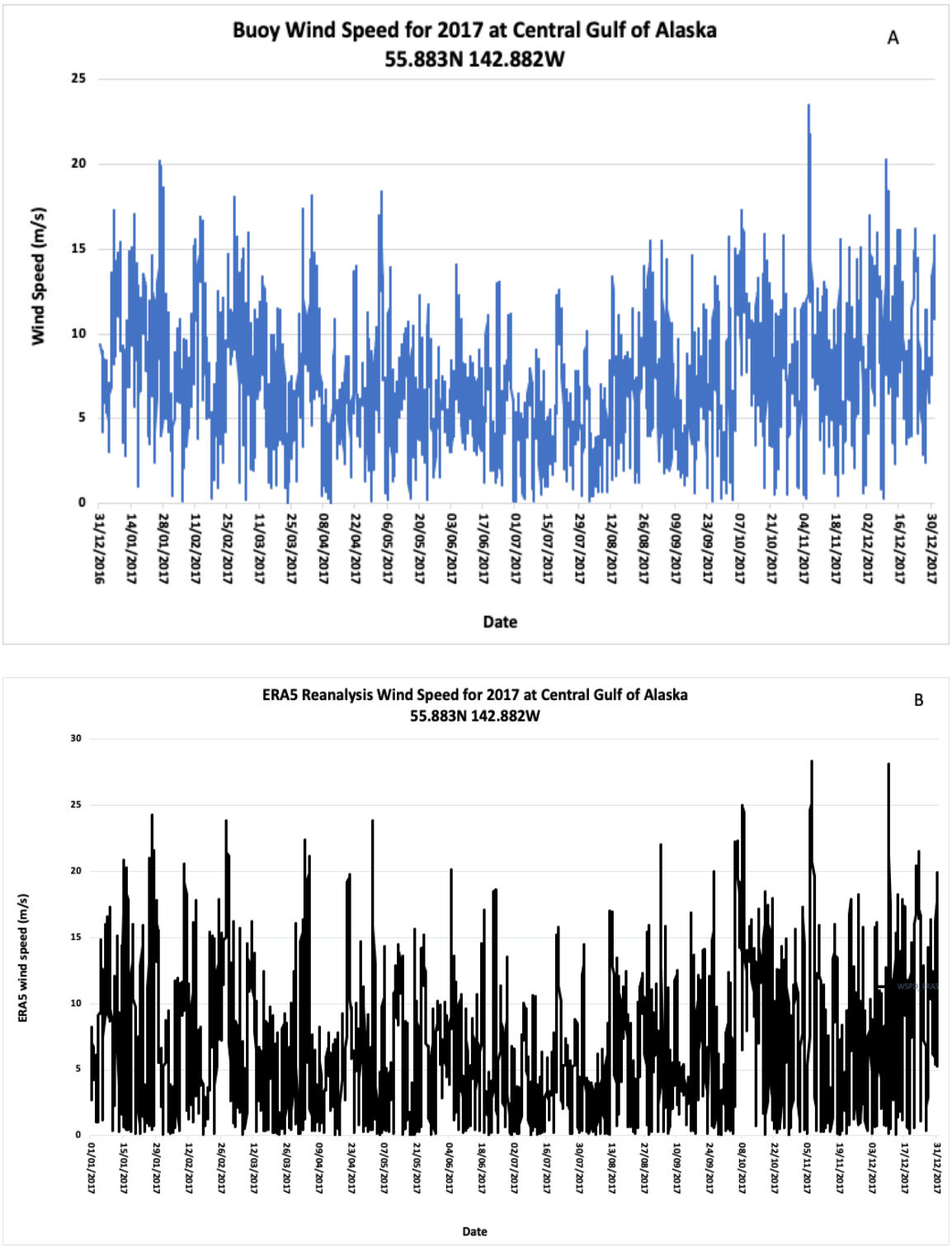

Figure 13. Panel A 2017 annual wind data collected by NOAA weather buoy for 2017. The data plotted is every hour for the entire year. The buoy from which the data was gathered has an overall height including the anemometers of five meter (NOAA, 2021) Panel B is the ERA5 reanalysis data for the same grid reference and period.

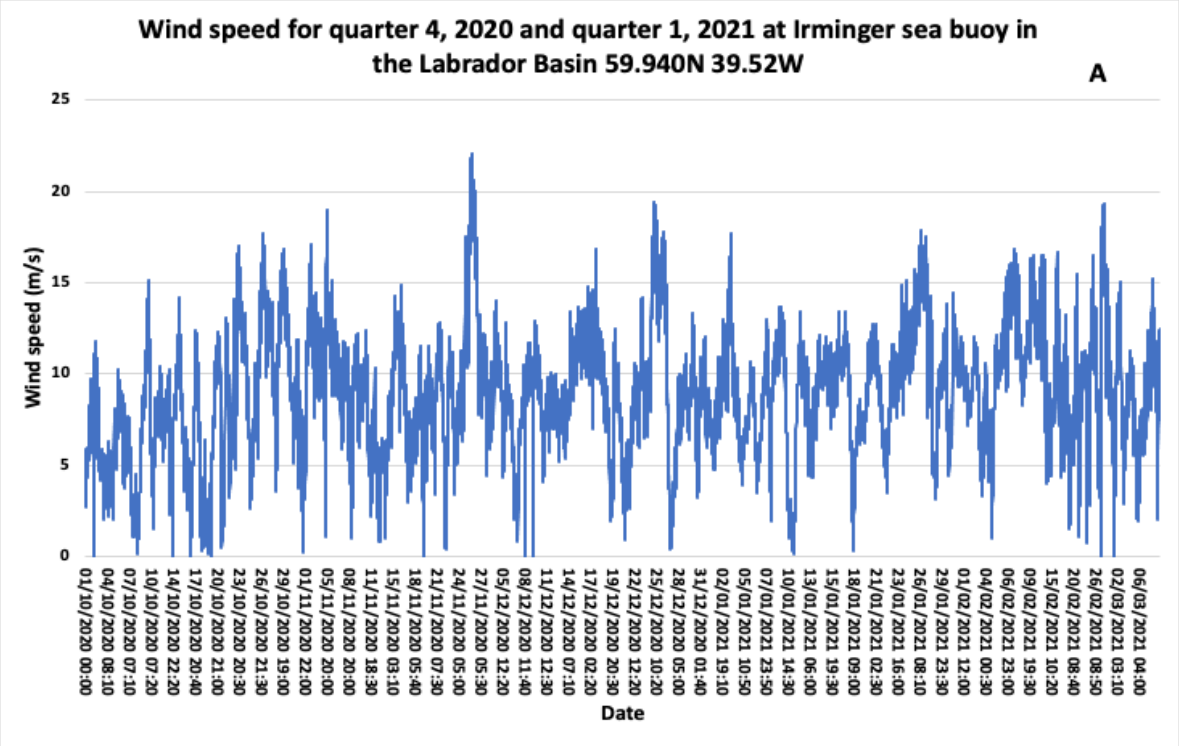

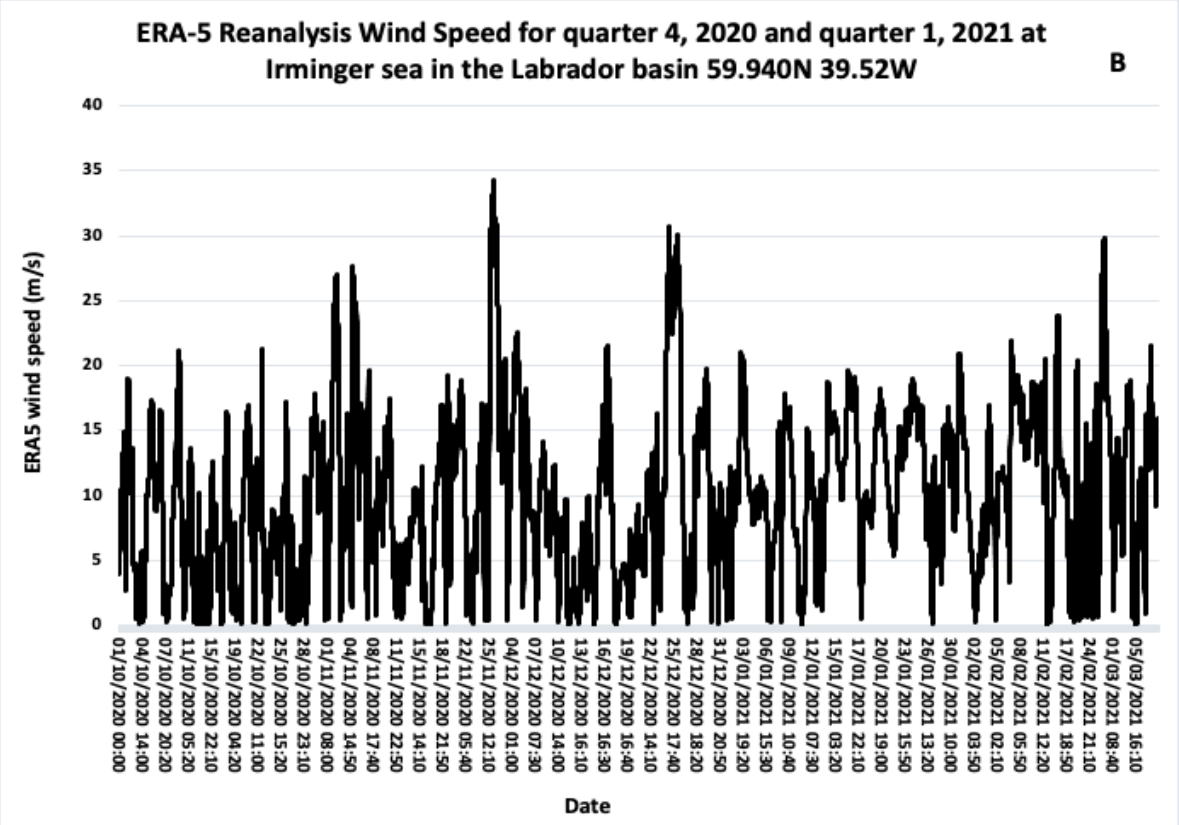

Figure 14. Panel A. The wind data collected by NOAA weather buoy for quarter 4 2020 and quarter 1 2021. The wind data plotted is every 10 minutes for this six-month period. Data either side of these two quarters was not captured by the buoy. The buoy from which the data was gathered has an overall height including the anemometers of five meters (NOAA, 2021) Panel B is the ERA5 Reanalysis data for same grid reference and period

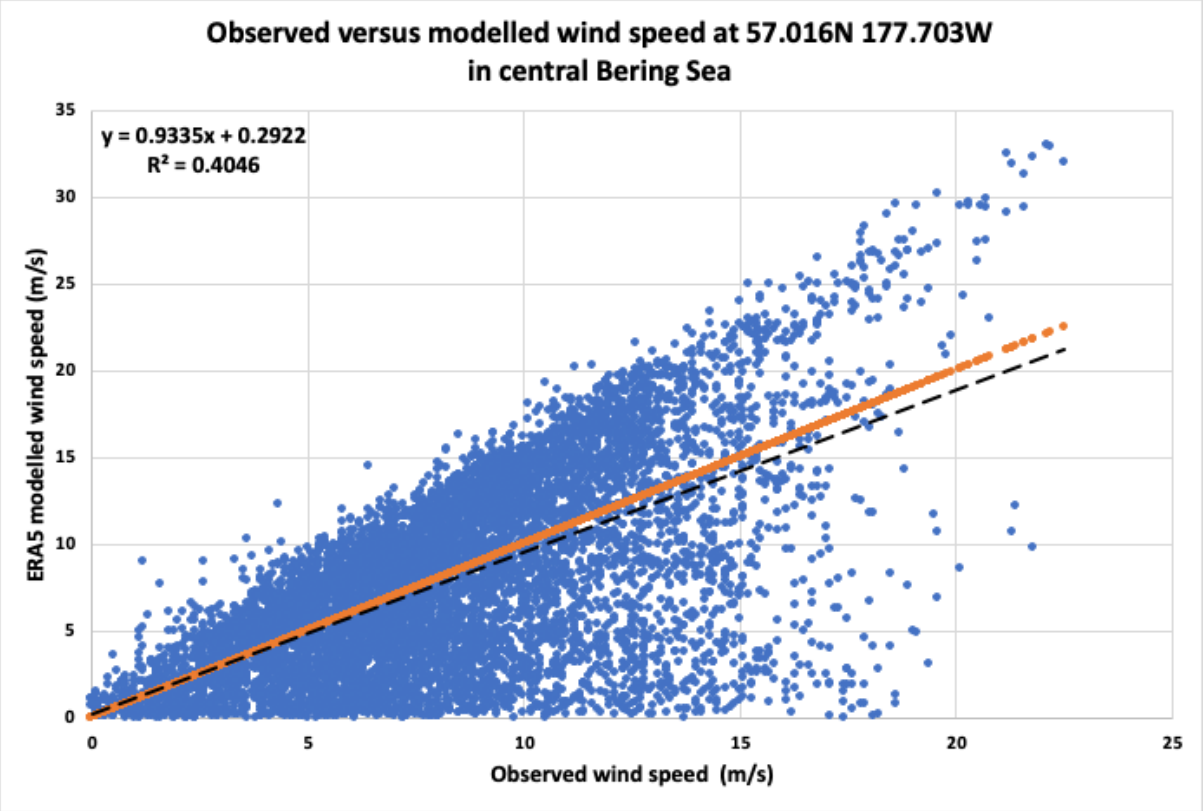

Figure 15. Scatterplot observed buoy collected data versus ERA-5 data in the Central Bering Sea for 2017

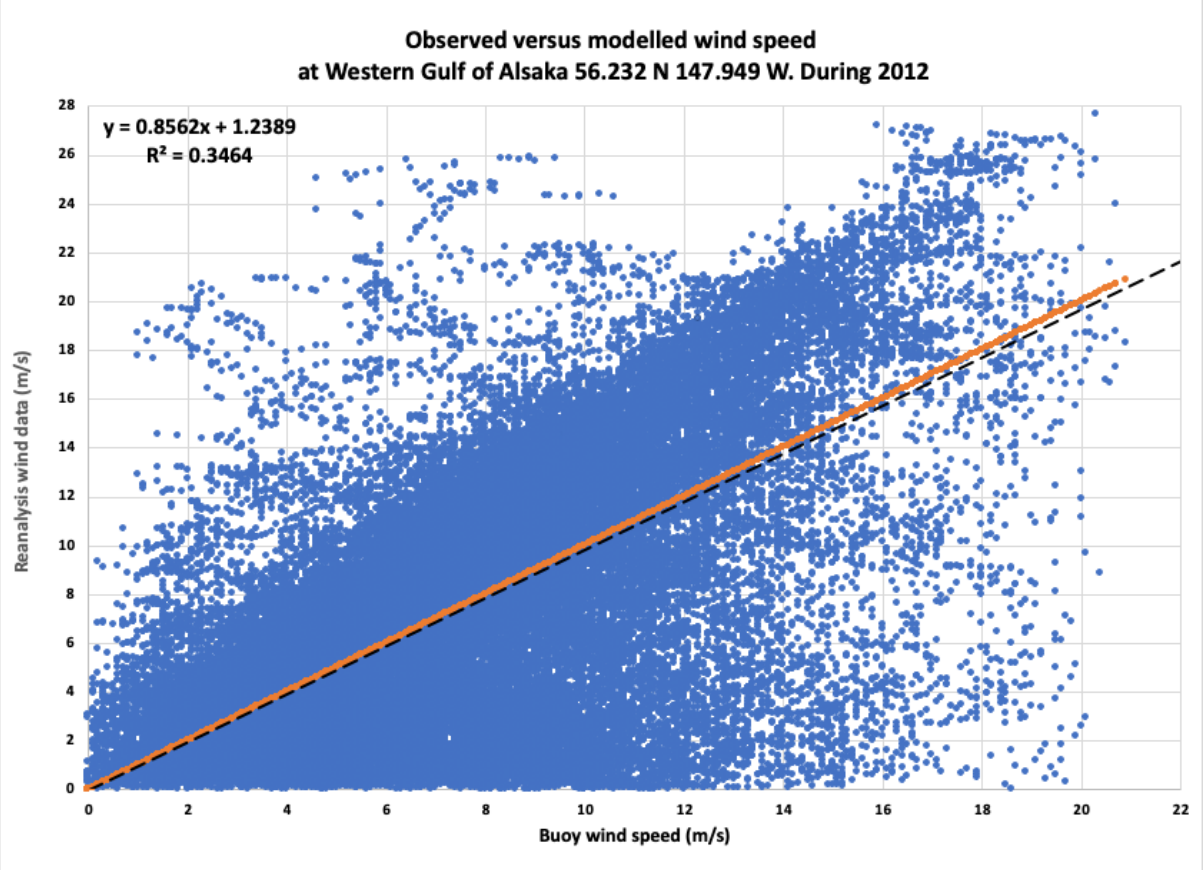

Figure 16. Scatterplot observed buoy collected data versus ERA-5 data in the Western Gulf of Alaska for 2011

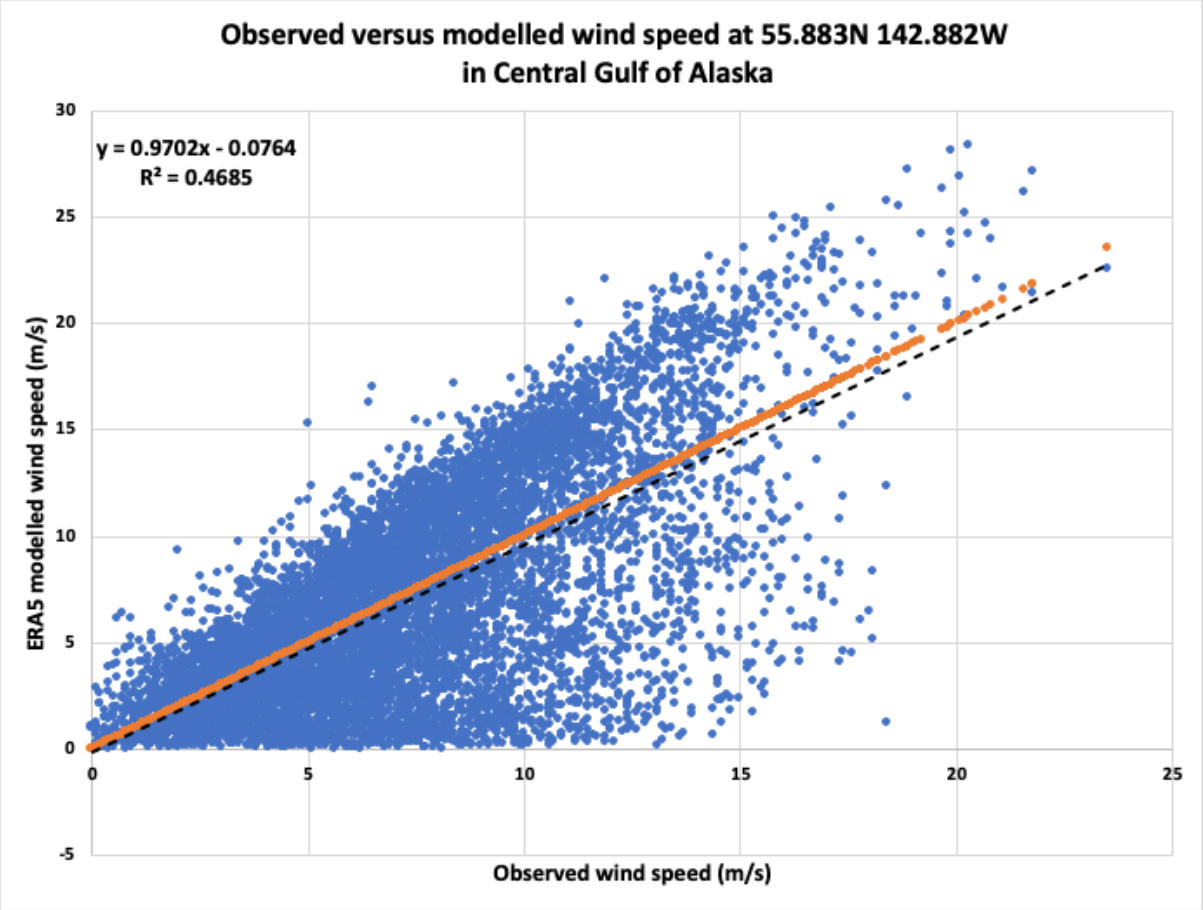

Figure 17. Scatterplot observed buoy collected data versus ERA-5 data in the Central Gulf of Alaska for 2017

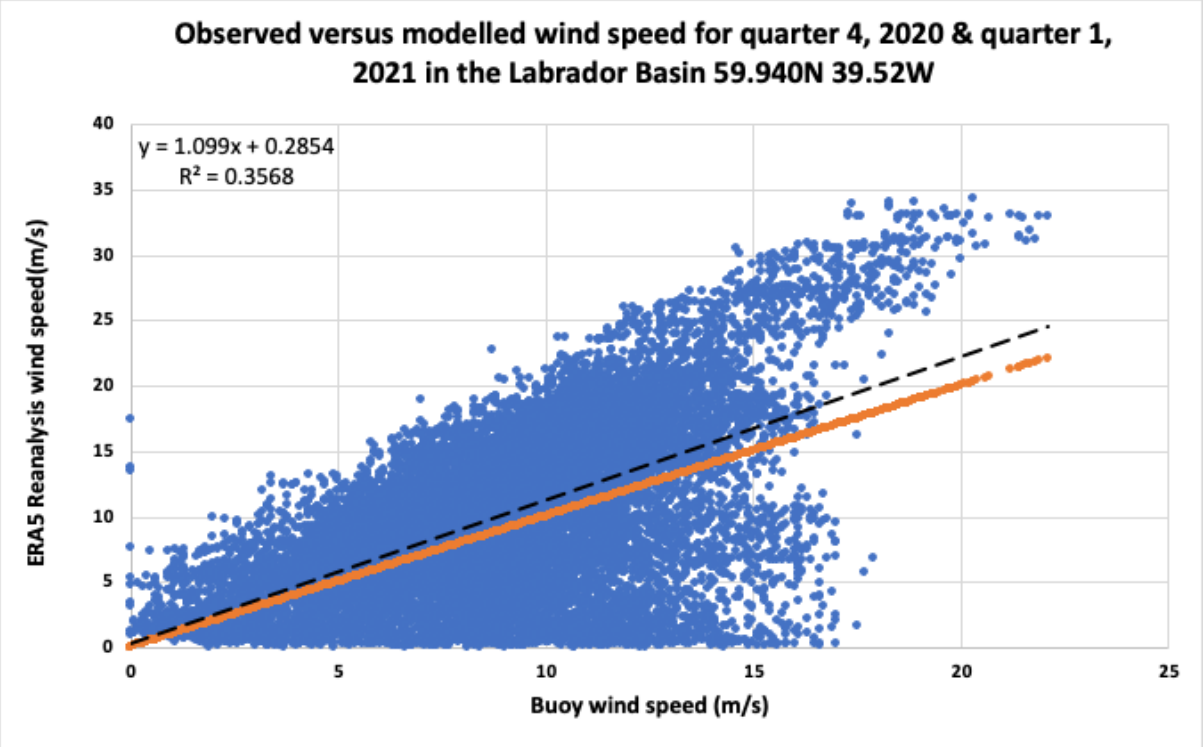

Figure 18. Scatterplot observed buoy collected data versus ERA-5 data in the Irminger Sea in the Labrador basin for quarter 4 2020 and quarter 1 2021